Structural diversity and luminescent sensing of three coordination polymers based on the hydrolysates of N,N′-bis(3,5-dicarboxylatophenyl)pyromelliticdi-imide)

Liming Fan [a], Jiang Wang [a], Li Zhao [a], Yujuan Zhang [a], Xiaoqing Wang [a], Tuoping Hu [a, *], Xiutang Zhang [b, **]

[a] Department of Chemistry, College of Science, North University of China, Taiyuan 030051, China
[b] Advanced Material Institute of Research, College of Chemistry and Chemical Engineering, Qilu Normal University, Jinan, 250013, China

ABSTRACT

Based on the hydrolysates of N,N′-bis(3,5-dicarboxylatophenyl)pyromelliticdi-imide) (H_4L) and 1,3-bis(imidazol-1-ylmethyl)benzene (bimb), three coordination polymers, namely, $\{[Zn(BTC)_{0.5}(bimb)]\cdot 4H_2O\}_n$ (**1**), $[Cu(BTC)_{0.5}(bimb)]_n$ (**2**), and $\{[Cd(AIP)(H_2O)]\cdot H_2O\}_n$ (**3**), have been obtained under solvothermal conditions. The possible hydrolysis mechanism of H_4L was investigated here. Structural analyses reveal that complex **1** is a 3D (4,4)-c $\{6^4.8^2\}\{6^6\}_2$-**bbf** net. Complex **2** displays a 2D 4-c $\{3^2.6^2.7^2\}$-**kgm** sheet. While complex **3** exhibits a 3D (3,6)-c $\{4.6^2\}_2\{4^2.6^{10}.8^3\}$-**rtl** net based on binuclear $\{Cd_2(COO)_4\}$ SBUs. Besides, luminescent sensing investigation indicated that **1** and **3** exhibit highly sensitive and selective sensing of chromate anions in aqueous solution.

© 2018 Elsevier B.V. All rights reserved.

1. Introduction

Coordination polymers (CPs), as an important branch of functional materials, have been widely investigated for their interesting structures and potential applications in the field of gas adsorption and separation, sensing and recognition, drug delivery and release, catalysis and photocatalysis, as well as fluorescent and nonlinear optical properties [1–8]. Such materials are generally assembled from organic linkers and metal nodes through coordination bonds and other weak interactions. As we all known, the construction of CPs are greatly effected by many factors [9–14]. Among them, there is no doubt that the design or the rational selection of organic linkers are the most important [15–17].

As the development of CPs, numerous organic linkers have been designed. It is noteworthy that some unexpected *in-situ* reactions of organic linkers, including decarboxylation, cycloaddition, oxidation/reduction, hydrolysis, may occur in the synthesis process, especially under hydrothermal or solvothermal conditions [18–22]. Take into consideration of high temperature and pressure, as well as the catalytic activity of metal ions, the *in-situ* reactions under hydrothermal or solvothermal conditions displaying another perspective to investigate the reaction mechanisms [23,24], for the coordination reaction between metal ions and generated organic linkers can frozen the *in-situ* reactions [25].

Recently, we designed CPs by using the ligand of N,N′-bis(3,5-dicarboxylatophenyl)pyromelliticdi-imide) (H_4L), fortunately or unfortunately, three CPs, namely, $\{[Zn(BTC)_{0.5}(bimb)]\cdot 4H_2O\}_n$ (**1**), $[Cu(BTC)_{0.5}(bimb)]_n$ (**2**), and $\{[Cd(AIP)(H_2O)]\cdot H_2O\}_n$ (**3**), were obtained based on the two hydrolysates (H_4BTC and H_2AIP, as shown in Scheme 1) of H_4L and 1,3-bis(imidazol-1-ylmethyl)benzene (bimb). The possible hydrolysis mechanism of H_4L was investigated. And structure analyses reveal that **1** is a 3D (4,4)-c $\{6^4.8^2\}\{6^6\}_2$-**bbf** net. Complex **2** displays a 2D 4-c $\{3^2.6^2.7^2\}$-**kgm** sheet. While **3** exhibits a 3D (3,6)-c $\{4.6^2\}_2\{4^2.6^{10}.8^3\}$-**rtl** net based on binuclear $\{Cd_2(COO)_4\}$ SBUs. Besides, the luminescent sensing of complexes **1** and **3** were investigated.

* Corresponding author.
** Corresponding author.
E-mail addresses: limingfan@nuc.edu.cn (L. Fan), hutuopingsx@126.com (T. Hu), xiutangzhang@163.com (X. Zhang).
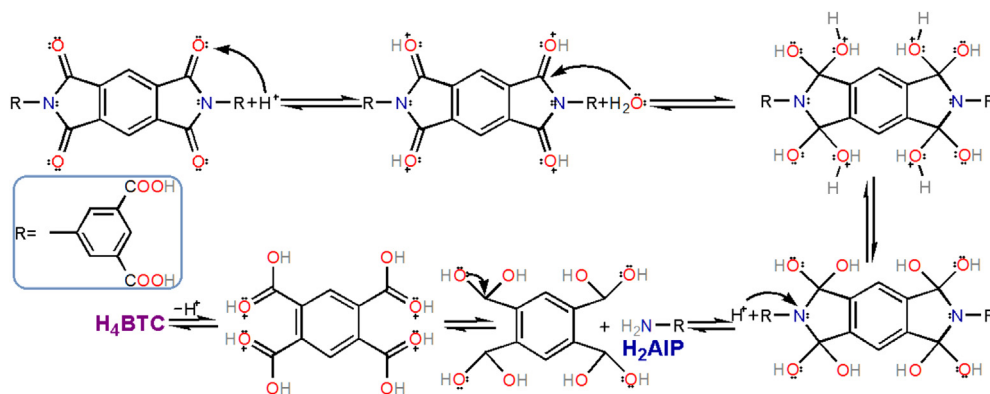
Scheme 1. The possible hydrolysis mechanism of H$_4$L.
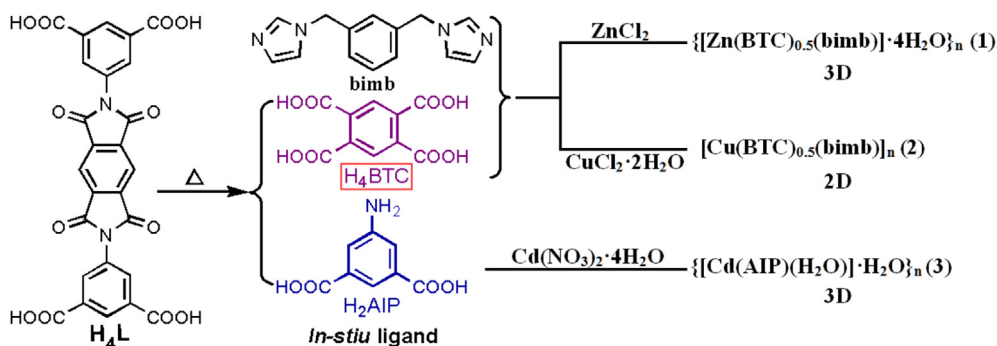
Scheme 2. Synthesis routes of complexes **1**–**3**.

2. Experimental

2.1. Materials and methods

Chemical reagents were purchased commercially and were used as received without further purification. Elemental analyses of C, N, and H were performed on an EA1110 CHNS-0 CE elemental analyzer. IR (KBr pellet) spectra were recorded on a Nicolet Magna 750FT-IR spectrometer. Thermogravimetric measurements were carried out in a nitrogen stream using a Netzsch STA449C apparatus with a heating rate of 10 °C min^{-1}. X-Ray powder diffraction (PXRD) was carried out on a RIGAKU DMAX2500 apparatus. Fluorescent data were collected on the Hitachi F-4600 FL Spectrophotometer.

2.2. Syntheses of complexes 1–3 (Scheme 2)

2.2.1. Synthesis of {[Zn(BTC)$_{0.5}$(bimb)]·4H$_2$O}$_n$ (1)

A mixture of ZnCl$_2$ (0.004 mmol), H$_4$L (0.002 mmol), bimb (0.004 mmol), and DMF/H$_2$O (1 mL, v/v = 1/1) were added to a hard glass tube, pumped into a near-vacuum, heated at 130 °C for 3 days, and then cooled to room temperature. The colorless crystals that formed was collected by filtration with the yield of **1** is 39% (based on Zn). Anal. (%) calcd. For C$_{19}$H$_{23}$N$_4$O$_8$Zn: C, 45.57; H, 4.63; N, 11.19. Found: C, 45.39; H, 4.69; N, 11.08. IR (KBr pellet, cm^{-1}): 3437 (s), 3129 (s), 2360 (m), 1616 (vs), 1326 (s), 1359 (vs), 1231 (m), 1096 (m), 1032 (w), 949 (m), 865 (w), 756 (m), 654 (m) (Fig. S1, see ESI).

2.2.2. Synthesis of [Cu(BTC)$_{0.5}$(bimb)]$_n$ (2)

A mixture of CuCl$_2$·2H$_2$O (0.008 mmol), H$_4$L (0.004 mmol), bimb (0.008 mmol), DMF/CH$_3$CN/H$_2$O (1 mL, v/v/v = 2/1/3), and one drop of HNO$_3$ aqueous solution (1.5 mM) were added to a hard glass

tube, pumped into a near-vacuum, and heated at 130 °C for 3 days, and then cooled to room temperature. The pink crystals that formed was collected by filtration with the yield of **2** is 43% (based on Cu). Anal. (%) calcd. for C$_{19}$H$_{15}$CuN$_4$O$_4$: C, 53.46; H, 3.54; N, 13.12. Found: C, 53.19; H, 3.56; N, 13.09. IR (KBr pellet, cm^{-1}): 3444 (m), 3129 (s), 2366 (m), 1583 (vs), 1526 (m), 1353 (vs), 1250 (m), 1102 (m), 955 (w), 865 (w), 814 (w), 718 (m), 654 (w), 544 (w) (Fig. S1, see ESI).

2.2.3. Synthesis of {[Cd(AIP)(H$_2$O)]·H$_2$O}$_n$ (3)

A mixture of Cd(NO$_3$)$_2$·4H$_2$O (0.008 mmol), H$_4$L (0.004 mmol), bimb (0.008 mmol), and DMF/CH$_3$CN/H$_2$O (1 mL, v/v/v = 1/1/2) were added to a hard glass tube, pumped into a near-vacuum, and heated at 130 °C for 3 days, and then cooled to room temperature. The pink crystals that formed was collected by filtration with the yield of **3** is 37% (based on Cd). Anal. (%) calcd. for C$_8$H$_9$CdNO$_6$: C, 29.33; H, 2.77; N, 4.28. Found: C, 29.38; H, 2.80; N, 4.27. IR (KBr pellet, cm^{-1}): 3277 (m), 1616 (m), 1558 (vs), 1372 (s), 1314 (s), 1231 (m), 1083 (m), 1025 (m), 968 (m), 782 (s), 730 (s), 654 (m) (Fig. S1, see ESI).

2.3. X-ray crystallography

Single crystals of **1**–**3** with appropriate dimensions were chosen under an optical microscope and quickly coated with high vacuum grease (Dow Corning Corporation) before being mounted on a glass fiber for data collection. Intensity data collection was carried out on a Siemens SMART diffractometer equipped with a CCD detector using Mo$K\alpha$ monochromatized radiation ($\lambda = 0.71073$ Å). The absorption correction was based on multiple and symmetry-equivalent reflections in the data set using the SADABS program.

The structures were solved by direct methods and refined by full-matrix least-squares using the SHELXTL package [26]. Anisotropic thermal parameters were applied to all non-hydrogen atoms. And all hydrogen atoms attached to C and N atoms were placed geometrically [27]. Crystallographic data for **1**−**3** are given in Table S1. Selected bond lengths and angles for **1**−**3** are listed in Table S2.

3. Result and discussion

3.1. Structure descriptions

3.1.1. Crystal structure of {[Zn(BTC)$_{0.5}$(bimb)]·4H$_2$O}$_n$ (**1**)

Although the structure as well as the luminescence in the solid state have been reported by Lin and co-workers before [28], we obtained it through the hydrolysis reaction of *N,N'*-bis(3,5-dicarboxylatophenyl)pyromelliticdi-imide) under solvothermal reaction and further investigated the luminescent sensing here. Complex **1** crystallizes in the monoclinic system, space group *P*2$_1$/*c* and the asymmetric unit contains one Zn^{II} ion, a half of BTC^{4-} ligands, one bimb linker, and four lattice water molecules (Fig. 1). Each Zn^{II} ion located in a distorted {ZnO$_2$N$_2$} tetrahedral geometry with τ_4 parameter is 0.89(8) ($\tau_4 = [360°-(\alpha+\beta)]/141°$, α and β are the two largest bond angles in the four-coordinate complexes.) [29], completed by two carboxyl O atoms from two different BTC^{4-} ligands, and two imidazolyl N atoms from two bimb linkers. Besides, the bond lengths of Zn−O/N are in the range of 1.993(0)−2.008(2) Å.

The H$_4$BTC is completely deprotonated and coordinated with four Zn^{II} ions by adopting (κ^1-κ^0)-(κ^1-κ^0)-(κ^1-κ^0)-(κ^1-κ^0)-μ_4 coordination mode (Mode I, Scheme 3). Four monodentate η^1 carboxyl groups of each BTC^{4-} ligand connected four Zn^{II} ions, leaving a 2D [Zn$_2$(BTC)]$_n$ **sql** sheet, with the nearest Zn···Zn distances being
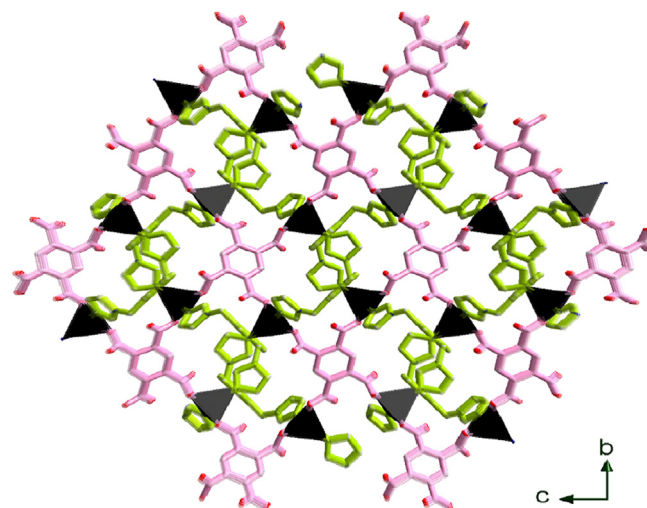

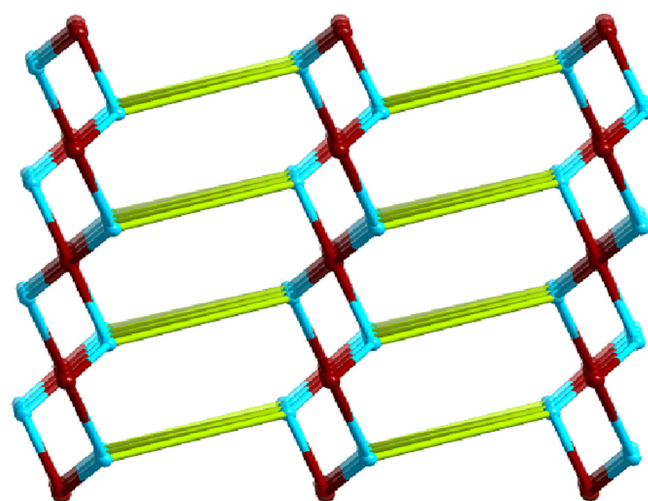**Fig. 2.** The 3D framework of **1** along *a* axis.

Fig. 3. The simplified binodal (4,4)-connected {6^4.8^2}{6^6}$_2$-**bbf** topology of **1**.

Fig. 1. The coordination environment of Zn(II) ion in **1** (Symmetry codes: A: *x*, 1/2−*y*, −1/2 + *z*; C: 1−*x*, −1/2 + *y*, −1/2−*z*; D: 1−*x*, 1/2 + *y*, −1/2−*z*; E: 2−*x*, −*y*, −*z*.).

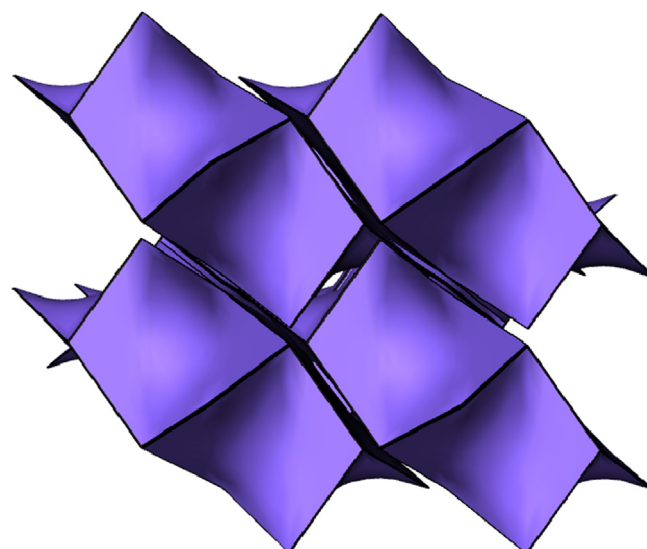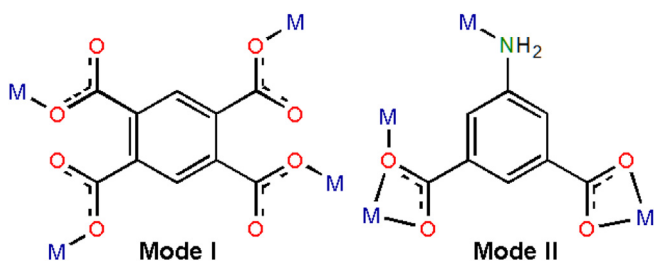**Scheme 3.** The coordination modes of H$_4$BTC/H$_2$AIP in **1** and **2**.

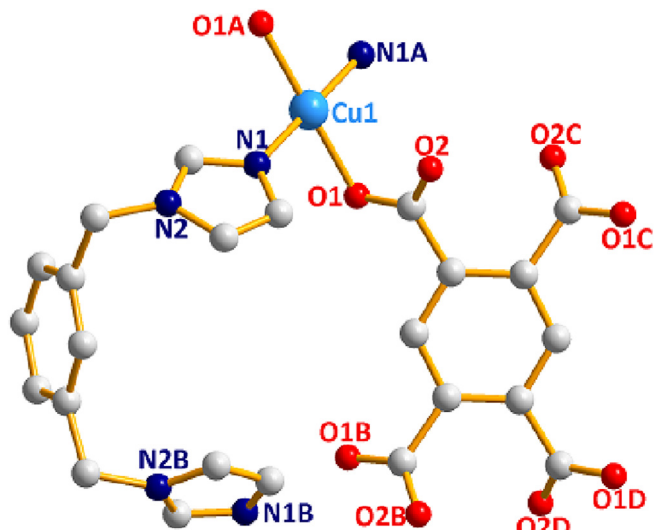**Fig. 4.** Tiling featured net for the framework of **1**.

Fig. 5. The coordination environment of Cu(II) in **2** (Symmetry codes: A: $1/2-x$, $1/2-y$, $-2-z$; B: x, $-y$, z; C: $1-x$, y, $-2-z$; D: $1-x$, $-y$, $-2-z$.).
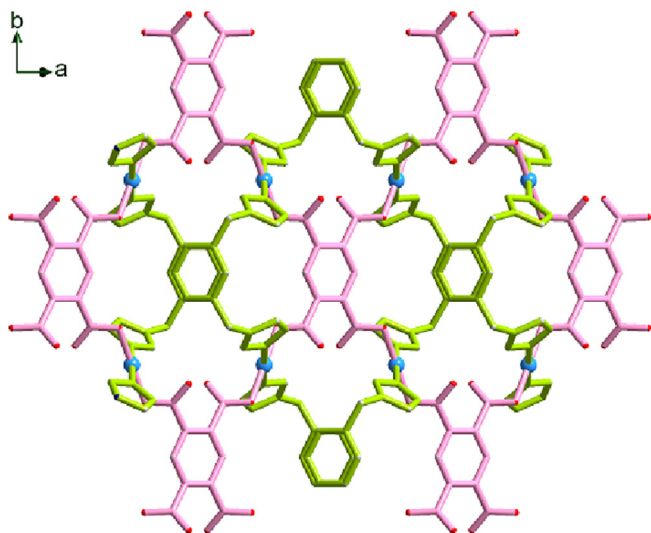

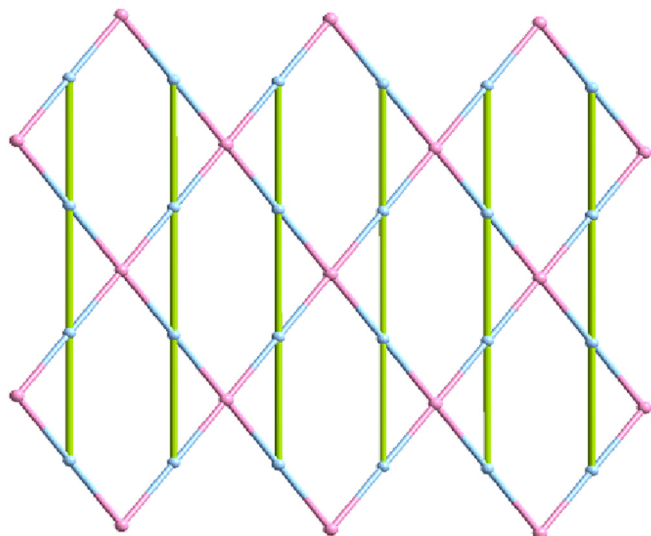**Fig. 6.** The 2D sheet of **2** view along c axis.

Fig. 7. The simplified 4-connected $\{3^2.6^2.7^2\}$-**kgm** sheet of **2**.
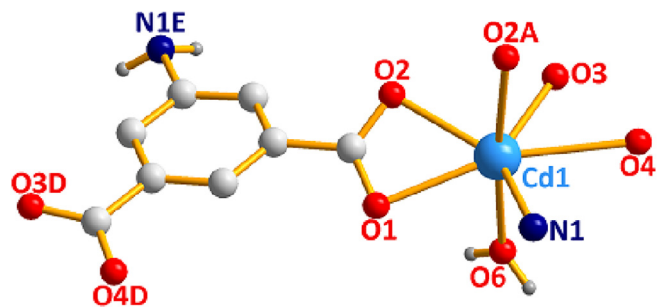

Fig. 8. The coordination environment of Cd(II) in **3** (Symmetry codes: A: $1-x$, $-y$, $1-z$; D: $-1+x$, y, z; E: $-1/2 + x$, $1/2-y$, $1/2 + z$.).
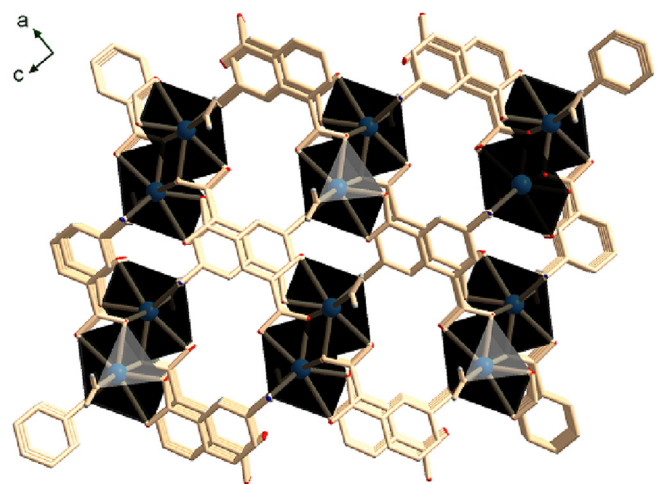
Fig. 9. The 3D network of **3** view along b axis.

6.212(8) Å, and 9.079(3) Å (Fig. S2). Besides, the bimb linkers bridged the adjacent Zn^{II} ions to form a 1D $[Zn(bimb)]_n$ polymeric chain (Fig. S3), with the bimb separated Zn···Zn distance is 11.705(2) Å. By sharing the central Zn^{II} ions, a 3D framework was constructed finally (Fig. 2). PLATON software revealed the porosity of **1** is 3.9% (88.3 out of the 2279.1 Å^3 unit cell volume) [30].

Fig. 10. The simplified binodal (3,6)-connected $\{4.6^2\}_2\{4^2.6^{10}.8^3\}$-**rtl** topology of **3**.

To illustrate the structure of **1**, the topological analysis approach is employed [31]. The final structure of **1** can be regard as a binodal 4,4-c net with stoichiometry (4-c)(4-c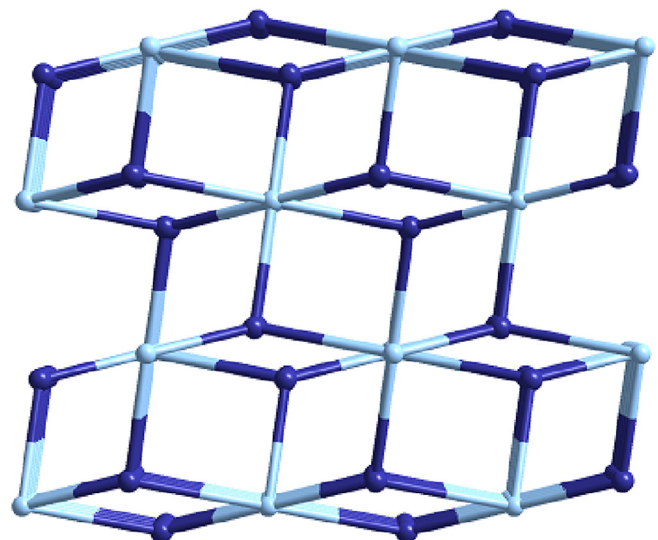)$_2$ by denoting both the Zn^{II} ions and BTC^{4-} ligands as 4-connected nodes (Fig. 3). And the Point (Schlafli) symbol for net is {$6^4.8^2$}{6^6}$_2$ with topological type being **bbf** (topos&RCSR.ttd). Further analysis of modular design reveals that the tiling of **1** is [6^8] = [$6a^2.6\,b^2.6c^4$] with the transitivity is 2331 (Figs. S4 and 4) [32].

3.1.2. Crystal structure of [Cu(BTC)$_{0.5}$(bimb)]$_n$ (**2**)

Structural analysis reveals that complex **2** crystallizes in the monoclinic system, space group $C2/m$ space group. As shown in Fig. 5, there are one Cu^{II} ion, half of BTC^{4-} ligands, and one bimb ligand in the asymmetric unit. Each Cu^{II} is tetra-coordinated, completed by two carboxyl O atoms from two BTC^{4-} ligands and two imidazolyl N atoms from two different bimb linkers, resulting in a perfect centrosymmetry {CuO$_2$N$_2$} parallelogram geometry with $\tau_4 = 0$. The bond distances of Cu–O are 2.002(2) Å, and Cu–N bond lengths are 1.963(8) Å, respectively.

In complex **2**, the H$_4$BTC adopted similar coordination mode (Mode I, Scheme 3) like that in complex **1**, linked with four Cu^{II} ions

Table 1
Comparisons of complexes **1** and **2**.

Complex	1	2
τ_4 of metal ion	0.89(8)	0
M-BTC	2D [Zn$_2$(BTC)]$_n$ sheet	2D [Cu$_2$(BTC)]$_n$ sheet
M-bimb	1D [Zn(bimb)]$_n$ chain	1D [Cu(bimb)]$_n$ chain
Structure	3D **bbf** net	2D **kgm** sheet
Topology	{$6^4.8^2$}{6^6}$_2$	{$3^2.6^2.7^2$}

through four monodentate (κ^1-κ^0)-μ_1 carboxyl groups. BTC^{4-} ligands connected with Cu^{II} ions to form a 2D [Cu$_2$(BTC)]$_n$ sheet with the adjacent Cu···Cu distances being 7.147(2) Å, and 8.498(7) Å (Fig. S5). At the same times, the bimb linkers bridged with Cu^{II} ions, obtaining an interesting 1D [Cu(bimb)]$_n$ chain with bimb separated Cu···Cu distance is 8.498(7) Å (Fig. S6). Shared with the Cu^{II} centers, the 1D [Cu(bimb)]$_n$ chains joined the 2D [Cu$_2$(BTC)]$_n$ sheets together, finally formed a 3D frameworks (Fig. 6). From a topology view, the Cu^{II} ions as well as the BTC^{4-} ligands both be simplified to 4-connected nodes, giving rise to a 4-connected **kgm** sheet with the Point (Schlafli) symbol of {$3^2.6^2.7^2$} for the final structure of **2** (Fig. 7).

3.1.3. Crystal structure of {[Cd(AIP)(H$_2$O)]·H$_2$O}$_n$ (**3**)

The crystal structure has been reported before [33], our novelties are the synthetic method of hydrolysis reaction of N,N′-bis(3,5-dicarboxylatophenyl)pyromelliticdi-imide under solvothermal reaction and its luminescent sensing. Structural analysis reveals that complex **3** crystallizes in the monoclinic system, space group $P2_1/n$ space group. As shown in Fig. 8, there are one Cd^{II} ion, one AIP^{2-} ligand, one coordinated water molecule, and one lattice water molecule in the asymmetric unit. Each Cd^{II} is hepta-coordinated, completed by six O atoms from three AIP^{2-} ligands and one coordinated water molecule, and one N atom from another AIP^{2-} ligand, resulting in a distorted {CdO$_6$N} pentagonal bipyramid geometry. The bond distances of Cd–O are in the range of 2.228(0)-2.662(3) Å, and Cd–N bond length is 2.243(5) Å, respectively.
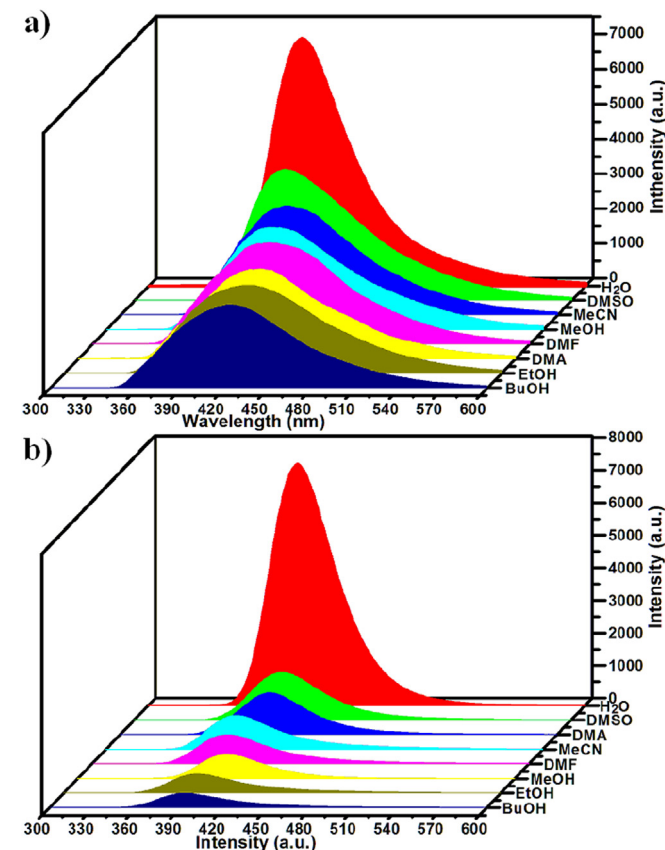

Fig. 11. The luminescence spectra of complexes **1** (a) and **3** (b) which were dispersed in different solvents.
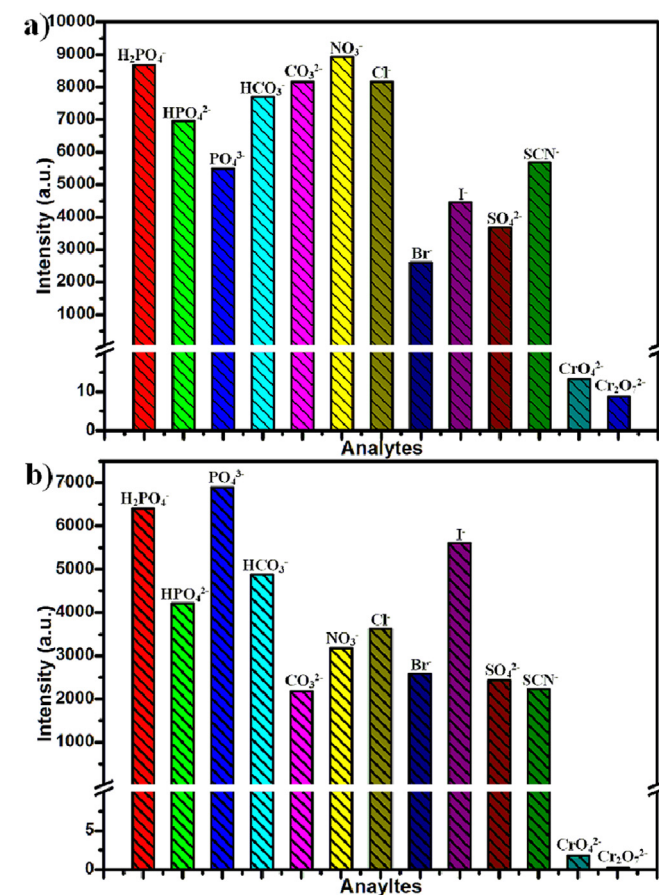

Fig. 12. The luminescence intensities of **1** (a) and **3** (b) which were dispersed in the aqueous solution of different anions.

In complex **3**, the H$_2$AIP is completely deprotonated and adopting $(\kappa^1$-$\kappa^1)$-$(\kappa^1$-$\kappa^2)$-κ^1N-μ_4 coordination mode (Mode II, Scheme 3) to coordinate with Cd^{II} ions. It is noteworthy that two chelating + bridging μ_2-η^2:η^1 carboxyl groups connected two CdII ions to form a binuclear {Cd$_2$(COO)$_4$} SBUs with the Cd···Cd distance is 3.794(4) Å (Fig. S7). Then each AIP^{2-} ligands linked with three {Cd$_2$(COO)$_4$} SBUs, finally constructed a 3D framework with 1D channels (Fig. 9). PLATON software revealed the porosity of **3** is 13.2% (126.0 out of the 953.1 Å^3 unit cell volume) after removal of solvents.

Topological analysis reveals that the final structure of **3** can be regard as a binodal 3,6-c net with stoichiometry with stoichiometry (3-c)$_2$(6-c) by denoting both the {Cd$_2$(COO)$_4$} SBUs and AIP^{2-} ligands as six-connected, and three-connected nodes, respectively (Fig. 10). And the Point (Schlafli) symbol for the net is {4.6^2}$_2${4^2.6^{10}.8^3} with the topological type being **rtl** (topos&RCSR.ttd).

3.2. Structure discussion

As shown in Scheme 1, the H$_4$L ligand hydrolyzed into two kinds hydrolysates of 1,2,4,5-benzenetetracarboxylic acid (H$_4$BTC), and 5-aminoisophthalic acid (H$_2$AIP) under solvothermal condition. Furthermore, the H$_4$BTC and H$_2$AIP reacted with metal salts in the presence of bimb linkers, finally leaving three CPs. Compared the above three CPs, we can found H$_4$BTC and H$_2$AIP ligands have competition effects when coordinating with metal ions. H$_4$BTC ligand offers a plane to connect metal ions, leaving 2D [M$_2$(BTC)]$_n$ sheets (Figs. S2 and S5, Table 1). And the auxiliary ligand of bimb can be further expanded the 2D layers into 3D networks. While the H$_2$AIP can provide a triangular pyramid skeleton to link metal ions, finally expanding into 3D architecture. Compared **1** and **2**, we can found the coordination preferences of metal ions make a huge change of the final framework, since the Zn^{II} ion tend to form a tetrahedron coordination geometry with $\tau_4 = 0.89(8)$ in **1**, and Cu^{II} ion lies in a planar quadrilateral with $\tau_4 = 0.00$ in **2**, respectively (Table 1). All in all, the coordination preferences of different metal ions determine the coordination reactions of H$_4$BTC/H$_2$AIP, and further ascertain the final structures of obtained CPs.

3.3. Powder X-ray diffraction and thermal analysis

To check the phase purity of these complexes, the PXRD patterns of title complexes were checked at room temperature. As shown in Fig. S8, the peak positions of the simulated and experimental PXRD patterns are in agreement with each other, demonstrating the good phase purity of the complexes. The dissimilarities in intensity may be due to the preferred orientation of the crystalline powder samples. The thermal stability experiments were performed on samples consisting of numerous single crystals under N$_2$ atmosphere with a heating rate of 10 °C min^{-1}, as shown in Fig. S9. The TGA curve of complex **1** displays steady weight loss in the temperature range of 90–140 °C (found 14.67%), corresponding to the loss of lattice water molecules (calcd. 14.38%). And then the framework can be exist stably until the temperature up to 380 °C. For **2**, there is no obviously weight loss before 320 °C, and a rapid

Fig. 13. Effect on the emission spectra of **1** dispersed in aqueous solution upon incremental addition of (a) CrO$_4^{2-}$ and (b) Cr$_2$O$_7^{2-}$ anions.

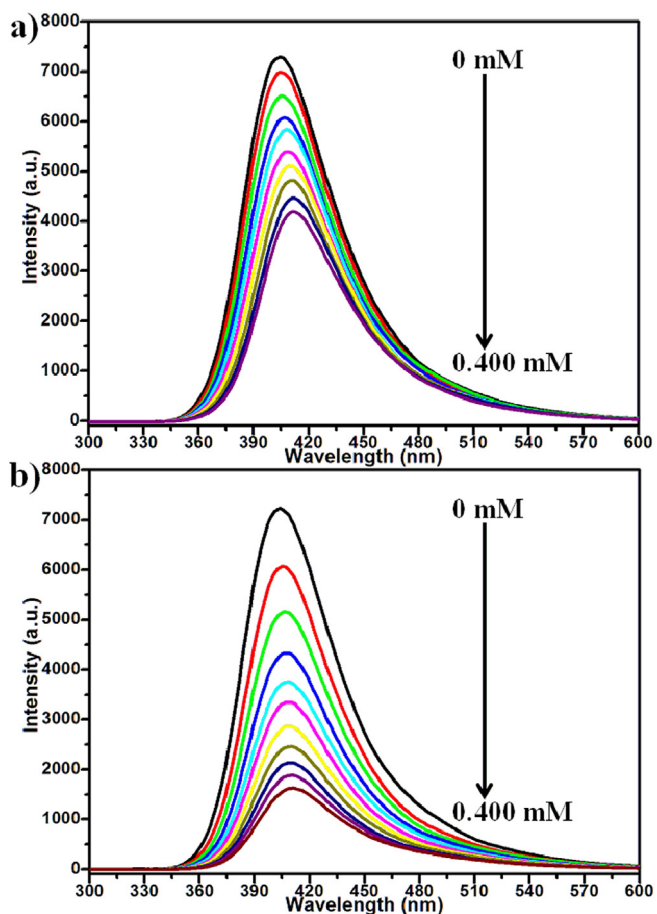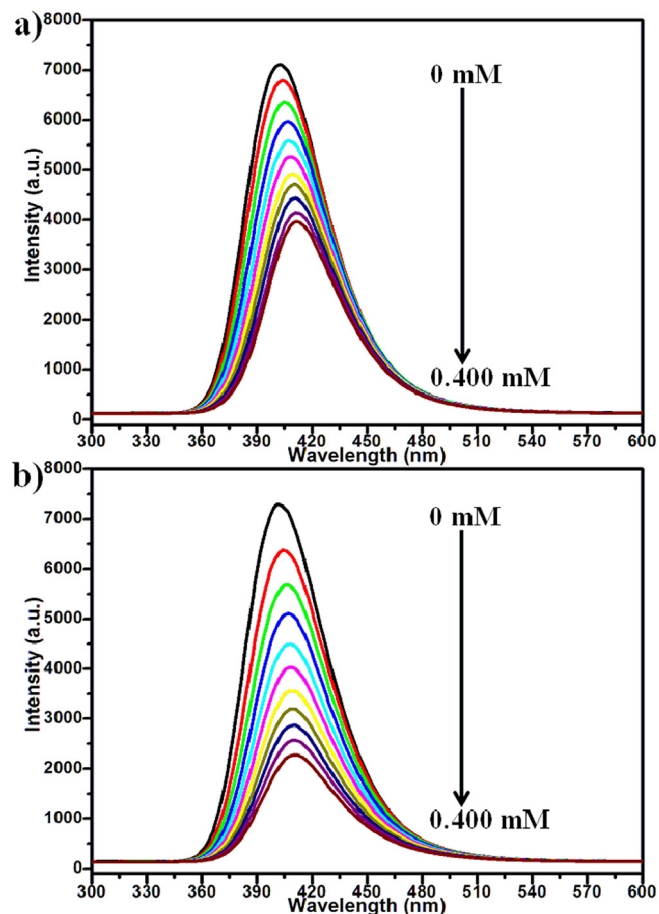**Fig. 14.** Effect on the emission spectra of **3** dispersed in aqueous solution upon incremental addition of (a) CrO$_4^{2-}$ and (b) Cr$_2$O$_7^{2-}$ anions.

weight loss can be found beyond this temperature, suggesting the decomposition of architecture. For **3**, the first weight loss of 10.67%, which occurred before 130 °C, corresponds to the release of lattice and coordinated water molecules (calcd. 11.00%), followed by a long plateau from 140 to 395 °C. And beyond 395 °C, there exists a rapid weight loss, suggesting the decomposition of architecture.

3.4. Luminescent sensing of chromate anions

The solid state luminescent spectra of complexes **1** and **3** were examined at room temperature, given in Fig. S10. Under the excitation wavelength of 325 nm, the emissions of complexes **1** and **3** exhibit strong blue-fluorescent emission peaks at 428 nm for **1**, and 396 nm for **3**, respectively. The emissions are neither metal-to-ligand charge transfer (MLCT) nor ligand-to-metal transfer (LMCT) for the Zn/Cd^{II} ions are difficult to oxidize or reduce due to their d^{10} configurations. Thus, they can be assigned to intraligand ($\pi^* \rightarrow n$ or $\pi^* \rightarrow \pi$) emission [34,35]. Eight kinds of solvent molecules, including DMA, DMF, DMSO, MeOH, MeCN, EtOH, BuOH, and H$_2$O, were selected to choose a suitable solvent in the following detection of anions. As shown in Figs. 11 and S11, after the finely ground samples of **1** and **3** (1 mg) were dispersed in 2 mL different solvents, those spectra displaying different luminescent intensities, the strongest in H$_2$O and the weakest in BuOH for both two CPs. Different emissions with distinct intensities in those solvents can be attributed to the weak interactions between the architectures and the guest solvent molecules [36,37]. Considering the strongest luminescent intensity in H$_2$O and the daily detection of waste water, the aqueous solutions were selected in the following tests.

For two CPs, the sensing of anions were performed by adding 1 mg finely ground samples into 2 mL 0.01 M aqueous solutions of thirteen different anions: K$_n$X (X = Cl$^-$, Br$^-$, I$^-$, NO$_3^-$, SO$_4^{2-}$, CO$_3^{2-}$, HCO$_3^-$, PO$_4^{3-}$, HPO$_4^{2-}$, H$_2$PO$_4^-$, SCN$^-$, CrO$_4^{2-}$, and Cr$_2$O$_7^{2-}$) at room temperature. As can be seen in Figs. 12 and S12, the luminescence intensities of X^{n-}@CPs suspensions are heavily dependent on the species of anions. And the Cr(IV) anions, CrO$_4^{2-}$, and Cr$_2$O$_7^{2-}$, exhibits extremely significant luminescent quenching effects.

To better understand the luminescence responses of two CPs to chromate anions, the relationships between the concentrations of chromate anions and the luminescence intensities were studied here. As shown in Figs. 13 and 14, with increasing addition of chromate anions, the intensities of luminescence intensities are steadily decrease with the quenching rates increasing (Figs. S13 and S14). In the concentration range of 0–0.4 mM, the I_0/I versus the concentrations of CrO$_4^{2-}$/Cr$_2$O$_7^{2-}$ anions can be well-fit to the nonlinear Stern–Volmer curves in exponential equations (in where, the I_0 and I are the luminescence intensities of the emulsions in the absence and presence of the chromate anions) (Fig. 15 and Table 2). And in the low concentration, the I_0/I versus the concentrations of chromate anions are fitted to the linear Stern–Volmer of $I_0/I-1=K_{sv}[Cr(IV)]+C$ (Fig. S15) [38,39]. Besides, the anti-interference

Table 2
Related parameters in the sensing of chromate anions in **1** and **3**.

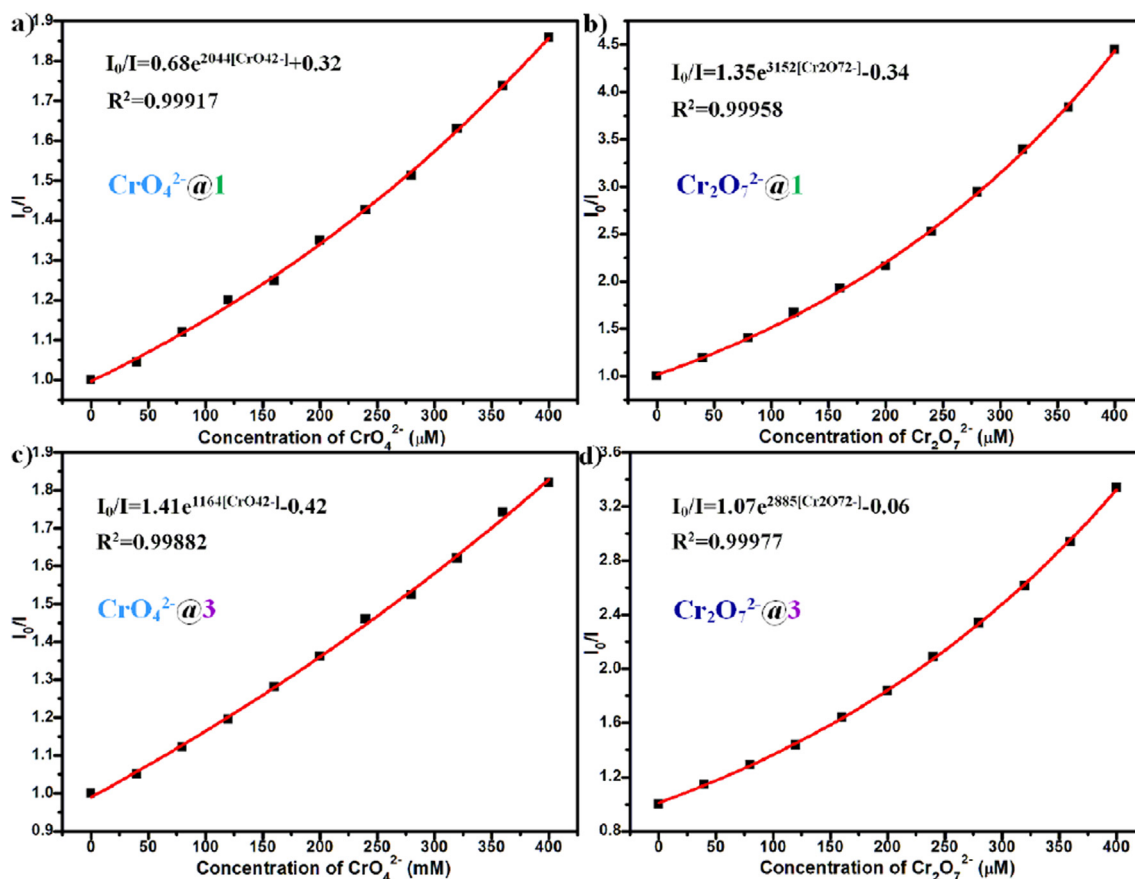|	Anion	Quenching rate	Exponential equation	K_{sv} (M^{-1})
1	CrO$_4^{2-}$	46.19%	$I_0/I = 0.68e^{2044[CrO42-]}+0.32$	1.57×10^3
	Cr$_2$O$_7^{2-}$	77.52%	$I_0/I = 1.35e^{3152[Cr2O72-]}-0.34$	5.97×10^3
3	CrO$_4^{2-}$	45.06%	$I_0/I = 1.41e^{1164[CrO42-]}-0.42$	1.84×10^3
	Cr$_2$O$_7^{2-}$	70.06%	$I_0/I = 1.07e^{2885[Cr2O72-]}-0.06$	4.17×10^3

Fig. 15. The plots of I_0/I versus concentrations of chromate anions in the series aqueous suspension of **1** and **3**.

abilities of two CPs for sensing chromate anions are displayed in Figs. S16 and S17, indicating both two CPs show good anti-interference abilities in detecting chromate anions from normal anions in aqueous solution. To further learn the recyclability of complexes **1** and **3** as sensor in detecting chromate anions, the quenching effects were tested for three cycles, and no evidently reduces being found (Fig. S18). After the tests, the PXRD patterns of the recycled samples are still well correspond with the simulated data of those CPs (Fig. S19). This phenomenon shows that complexes **1** and **3** may be good candidates to detect chromate anions.

The possible luminescence quenching mechanism of two CPs for chromate anions were investigated here. UV–vis absorption spectra of chromate anions in aqueous solution was recorded. As shown in Fig. S20, chromate anions in aqueous solution both show two broad absorption bands are 258 and 360 nm for $Cr_2O_7^{2-}$ and 273 and 372 nm for CrO_4^{2-} anion, which cover the absorption bands of the complex **1** (210–340 nm), complex **3** (210–360 nm), indicating that there are competitive absorptions of the exciting light between the chromate anions and CPs. Hence, the luminescence quenching by chromate anions may be the process involving competitive absorption on light excitation between the chromate anions and the CPs as well as energy resonance transfer from the frameworks of complexes **1** and **3** to chromate anions [40–43].

4. Conclusion

In summary, three CPs were obtained based on the hydrolysates of *N,N′*-bis(3,5-dicarboxylatophenyl)pyromelliticdi-imide) (H$_4$L), 1,2,4,5-benzenetetracarboxylic acid (H$_4$BTC), and 5-aminoisophthalic acid (H$_2$AIP) and 1,3-bis(imidazol-1-ylmethyl) benzene (bimb). The possible hydrolysis mechanism of H$_4$L was investigated. And structure analyses reveal the structures ranged from 3D **bbf** net for **1**, 2D **kgm** sheet for **2**, and 3D **rtl** net for **3**, respectively. And the luminescent sensing investigation indicating complexes **1** and **3** exhibit highly sensitive and selective sensing of $CrO_4^{2-}/Cr_2O_7^{2-}$ anions in aqueous solution through strong luminescence quenching effects. Further investigation of *N,N′*-bis(3,5-dicarboxylatophenyl)pyromelliticdi-imide) in the anhydrous environments are underway in our lab.

Acknowledgements

Appendix A. Supplementary data

Supplementary data related to this article can be found at https://doi.org/10.1016/j.molstruc.2018.05.092.

References

[1] A. Proust, B. Matt, R. Villanneau, G. Guillemot, P. Gouzerh, G. Izzet, Chem. Soc. Rev. 41 (2012) 7605.
[2] Y.–B. Huang, J. Liang, X.–S. Wang, R. Cao, Chem. Soc. Rev. 46 (2017) 126.
[3] H.C. Zhou, J.R. Long, O.M. Yaghi, Chem. Rev. 112 (2012) 673.
[4] Z. Hu, B.J. Deibert, J. Li, Chem. Soc. Rev. 43 (2014) 5815.
[5] A. Rossin, G. Tuci, L. Luconi, G. Giambastiani, ACS Catal. 7 (2017) 5035.
[6] F. Wang, S. Kusaka, Y. Hijikata, N. Hosono, S. Kitagawa, ACS Appl. Mater. Interfaces 9 (2017) 33455.
[7] L.-Y. Guo, H.-F. Su, M. Kurmoo, C.-H. Tung, D. Sun, L.-S. Zheng, J. Am. Chem. Soc. 139 (2017) 14033.
[8] L. Chen, J.-W. Ye, H.-P. Wang, M. Pan, S.-Y. Yin, Z.-W. Wei, L.-Y. Zhang, K. Wu, Y.-N. Fan, C.-Y. Su, Nat. Commun. 8 (2017) 15985.
[9] R.M. Marti, J.D. Howe, C.R. Morelock, M.S. Conradi, K.S. Walton, D.S. Sholl, S.E. Hayes, J. Phys. Chem. C 121 (2017) 25778.
[10] H. Wang, F.-Y. Yi, S. Dang, W.-G. Tian, Z.-M. Sun, Cryst. Growth Des. 14 (2014) 147.
[11] A.M. Ullman, J.W. Brown, M.E. Foster, F. Léonard, K. Leong, V. Stavila, M.D. Allendorf, Inorg. Chem. 55 (2016) 7233.
[12] M. Arıcı, O.Z. Yeşilel, O. Büyükgüngör, Y. Yerli, Polyhedron 142 (2018) 9.
[13] J.-Y. Liang, G.-P. Li, R.-C. Gao, N.-N. Bai, W.-Q. Tong, L. Hou, Y.-Y. Wang, Cryst. Growth Des. 17 (2017) 6733.
[14] Z.-L. Wu, J. Dong, W.-Y. Ni, B.-W. Zhang, J.-Z. Cui, B. Zhao, Inorg. Chem. 54 (2015) 5266.
[15] M. Arıcı, O.Z. Yeşilel, M. Taş, Cryst. Growth Des. 15 (2015) 3024.
[16] W.-M. Chen, X.-L. Meng, G.-L. Zhuang, Z. Wang, M. Kurmoo, Q.-Q. Zhao, X.-P. Wang, B. Shan, C.-H. Tung, D. Sun, J. Mater. Chem. 5 (2017) 13079.
[17] Y.-L. Wu, F.-S. Guo, G.-P. Yang, L. Wang, J.-C. Jin, X. Zhou, W.-Y. Zhang, Y.-Y. Wang, Inorg. Chem. 55 (2016) 6592.
[18] T. Hu, W. Bai, X. Hu, X. Zhao, X. Wang, Cryst. Growth Des. 10 (2010) 3324.
[19] G.-B. Li, J.-M. Liu, Z.-Q. Yu, W. Wang, C.-Y. Su, Inorg. Chem. 48 (2009) 8659.
[20] Y.-F. Zeng, X. Hu, L. Xue, S.-J. Liu, T.-L. Hu, X.-H. Bu, Inorg. Chem. 51 (2012) 9571.
[21] V. Bon, I. Senkovska, D. Wallacher, D.M. Többens, I. Zizak, R. Feyerherm, U. Mueller, S. Kaskel, Inorg. Chem. 53 (2014) 1513.
[22] T. Wen, D.-X. Zhang, J. Zhang, Inorg. Chem. 52 (2013) 12.
[23] A.K. Gupta, A.K. Srivastava, I.K. Mahawar, R. Boomishankar, Cryst. Growth Des. 14 (2014) 1701.
[24] P. Lama, P.K. Bharadwaj, Cryst. Growth Des. 11 (2011) 5434.
[25] L. Fan, W. Fan, B. Li, X. Liu, X. Zhao, X. Zhang, Dalton Trans. 44 (2015) 2380.
[26] G.M. Sheldrick, SHELXS-97, Program for Solution of Crystal Structures, University of Göottingen, Germany, 1997.
[27] G.M. Sheldrick, Acta Crystallogr. A64 (2008) 112.
[28] J.-D. Lin, J.-W. Chen, S.-W. Du, Cryst. Growth Des. 8 (2008) 3345.
[29] L. Yang, D.R. Powell, R.P. Houser, Dalton Trans. (2007) 955.
[30] A.L. Spek, Acta Crystallogr. D. 65 (2009) 148.
[31] V.A. Blatov, Struct. Chem. 23 (2012) 955.
[32] M. O'Keeffe, M.A. Peskov, S.J. Ramsden, O.M. Yaghi, Acc. Chem. Res. 41 (2008) 1782.
[33] J. Tao, X. Yin, Y.-B. Jiang, R.-B. Huang, L.-S. Zheng, Inorg. Chem. Commun. 6 (2003) 1171.
[34] X. Zhang, L. Fan, W. Fan, B. Li, X. Zhao, CrystEngComm 17 (2015) 6681.
[35] Y. Yang, K.-Z. Wang, D. Yan, ACS Appl. Mater. Interfaces 9 (2017) 17399.
[36] L. Fan, W. Fan, B. Li, X. Zhao, X. Zhang, CrystEngComm 17 (2015) 9413.
[37] Y. Li, X. Zhang, W. Chen, W. Shi, P. Cheng, Inorg. Chem. 56 (2017) 11768.
[38] L. Zhang, Z. Kang, X. Xin, D. Sun, CrystEngComm 18 (2016) 193.
[39] W.-M. Chen, X.-L. Meng, G.-L. Zhuang, Z. Wang, M. Kurmoo, Q.-Q. Zhao, X.-P. Wang, B. Shan, C.-H. Tung, D. Sun, J. Mater. Chem. 5 (2017) 13097.
[40] G.-X. Wen, M.-L. Han, X.-Q. Wu, Y.-P. Wu, W.-W. Dong, J. Zhao, D.-S. Li, L.-F. Ma, Dalton Trans. 45 (2016) 15492.
[41] B. Yan, Acc. Chem. Res. 50 (2017) 2789.
[42] H.N. Chang, S.X. Hou, Z.C. Hao, G.H. Cui, Polyhedron 141 (2018) 276.
[43] F.-L. Yuan, Y.-Q. Yuan, M.-Y. Chao, D.J. Young, W.-H. Zhang, J.-P. Lang, Inorg. Chem. 56 (2017) 6522.